Coordinate space proton-deuteron scattering calculations including Coulomb force effects

S. Ishikawa*

Department of Physics, Science Research Center, Hosei University, 2-17-1 Fujimi, Chiyoda, Tokyo 102-8160, Japan

(Received 5 June 2009; revised manuscript received 9 August 2009; published 18 November 2009)

We present a practical method to solve the proton-deuteron scattering problem at energies above the three-body breakup threshold, in which we treat three-body integral equations in coordinate space accommodating long-range proton-proton Coulomb interactions. The method is examined for phase shift parameters and then applied to calculations of differential cross sections in elastic and breakup reactions, analyzing powers, etc., with a realistic nucleon-nucleon force and three-nucleon forces. The effects of the Coulomb force and the three-nucleon forces on these observables are discussed in comparison with experimental data.

DOI: 10.1103/PhysRevC.80.054002 PACS number(s): 25.10.+s, 21.45.Ff

I. INTRODUCTION

Scattering observables of three-nucleon ($3N$) systems, proton-deuteron (pd) scattering and neutron-deuteron (nd) scattering, are good sources of information about unknown aspects of the nuclear forces such as off-shell differences in nucleon-nucleon force (2NF) models and possible evidence of $3N$ forces (3NFs). Because of the technical advantage of treating charged particles as beam, target, or detected particles over using neutral ones, the available data sets of the pd reaction are richer both in quantity and quality than those of the nd reaction. However, because of a mathematical difficulty in treating three-body systems with long-range Coulomb interactions, a precise calculation of the pd scattering, especially for energies above the three-body breakup threshold (TBT), is one of the most challenging subjects in physics of few-body systems.

In the last decade, some developments have been made in this problem by calculations based on the Kohn variational principle [1,2] and on the momentum space Faddeev equations [3] using the screening and renormalization method [4–7].

In this article, we present another approach to the pd scattering problem, which is based on integral equations for wave functions in coordinate space. Calculations by this approach for non-Coulombnic $3N$ systems with realistic 2NFs and 3NFs were performed for ^{3}H in Refs. [8,9] and for the nd scattering at energies above the TBT in Refs. [10–12]. A direct application of the Faddeev equation to Coulombnic $3N$ systems, namely, the ^{3}He bound state and the pd scattering, is known to bring a severe singularity to the integral kernel due to the long-range character of the proton-proton (pp) Coulomb force. In Ref. [13], Sasakawa and Sawada proposed a modification of the Faddeev equation to treat the singularity by introducing auxiliary potentials that act between charged spectator particles and the center of mass (c.m.) of the rest pair particles. Because we use an iterative method to solve the integral equations, in which one needs to operate the integral kernel on known functions repeatedly, it is essential to establish an accurate kernel operation for precise calculations. In the integral kernel of this Coulomb-modified Faddeev equation, which will be referred to as the SSF equation, the singularity due to the pp Coulomb potential is expected to be canceled by the auxiliary potentials, on the condition that three particles are bound or that no three-body breakup channel is open. Solutions of the SSF equation were successfully obtained for the ^{3}He bound state in Refs. [14–16] and for the pd scattering at energies *below* the TBT in Refs. [17,18]. However, the cancellation is not trivially expected when a three-body breakup channel opens. In this article, we treat this problem and show how our approach practically is applicable for pd scattering *above* the TBT.

The next section is devoted to presenting the notation used in this article and to introducing the SSF equation for the pd scattering in integral equation form. In Sec. III, we analyze a problem in the integral kernel of the SSF equation due to the pp Coulomb force and propose a method to perform numerical calculations. Then, some numerical results for pd and nd scattering using a realistic 2NF and 3NFs are presented in Sec. IV. A summary is given in Sec. V. Our iterative method [8,19] is reviewed in Appendix A, and some useful functions and formulas are given in Appendices B and C.

II. THREE-BODY SCATTERING EQUATION WITH COULOMB FORCE EFFECTS

In this section, we describe our notation and present the SSF equation by taking a proton(1)-proton(2)-neutron(3) system as an example. We do not consider spins' degrees of freedom, angular momentum dependence of the potentials, or 3NFs in describing our formalism because of simplicity. The deuteron thus is supposed to be an s-wave proton-neutron (pn) bound state with energy E_d. We use sets of coordinate systems $\{\boldsymbol{x}_k, \boldsymbol{y}_k\}$ (the Jacobi coordinates) to describe the three-body system defined as

$$\boldsymbol{x}_k = \boldsymbol{r}_i - \boldsymbol{r}_j, \qquad \boldsymbol{y}_k = \boldsymbol{r}_k - \tfrac{1}{2}(\boldsymbol{r}_i + \boldsymbol{r}_j), \tag{1}$$

where (i, j, k) denote $(1, 2, 3)$ or their cyclic permutations and $\boldsymbol{r}_i$ is the position vector of the particle i (see Fig. 1). Subscripts to indicate particles are omitted when there is no confusion.

We write a three-body Hamiltonian in the c.m. frame as

$$H = H_0 + V_1 + V_2 + V_3, \tag{2}$$

*ishikawa@hosei.ac.jp

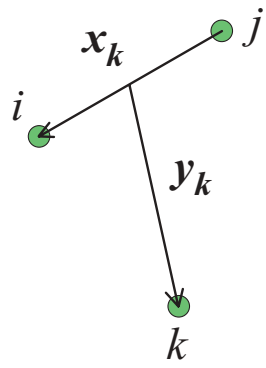

FIG. 1. (Color online) The Jacobi coordinates of the three-body system.

where H_0 is the internal kinetic energy operator of the three-body system,

$$H_0 = T_x(\boldsymbol{x}) + T_y(\boldsymbol{y}) = -\frac{\hbar^2}{m}\nabla_x^2 - \frac{3\hbar^2}{4m}\nabla_y^2, \tag{3}$$

with nucleon mass m, and V_k is a potential to describe the interaction between particles i and j consisting of a short-range nucleon-nucleon potential (2NP) $V_k^S(x_k)$ and the pp Coulomb potential $V^C(x_3)$ $(=e^2/x_3^2)$:

$$V_k = V_k^S(x_k) + \delta_{k,3}V^C(x_3). \tag{4}$$

We begin with a differential form of the SSF equation for a three-body c.m. energy $E(>0)$ [13],

$$\left[E - H_0 - V_1^S - u^C(y_1)\right]\Phi_1 = [\Delta\Phi]_1\,, \tag{5a}$$
$$\left[E - H_0 - V_2^S - u^C(y_2)\right]\Phi_2 = [\Delta\Phi]_2\,, \tag{5b}$$
$$\left[E - H_0 - V_3^S - V^C(x_3)\right]\Phi_3 = [\Delta\Phi]_3\,, \tag{5c}$$

where Φ_k's are Faddeev components and $u^C(y_k)$ is an auxiliary Coulomb potential acting between the particle k and the c.m. of the pair ij,

$$u^C(y_k) = \frac{e^2}{y_k} \quad (k = 1, 2). \tag{6}$$

The symbols $[\Delta\Phi]_k$ in the right-hand side denote

$$[\Delta\Phi]_k \equiv \begin{cases} V_k^S(\Phi_i + \Phi_j) & (k = 1, 2), \\ V_3^S(\Phi_1 + \Phi_2) + [V^C(x_3) - u^C(y_1)]\Phi_1 & \\ \quad + [V^C(x_3) - u^C(y_2)]\Phi_2 & (k = 3). \end{cases} \tag{7}$$

The auxiliary potentials play different roles on each side of Eqs. (5a)–(5c). On the left-hand side of Eqs. (5a) and (5b), these potentials work to distort the spectator proton from a free state [see Eq. (14)]. On the right-hand side of Eq. (5c), that is, in $[\Delta\Phi]_3$, the auxiliary potential is expected to cancel out the long-rangeness of the pp Coulomb potential V^C. The latter point is discussed later in this article. It should be noted that the auxiliary potentials in Eqs. (5a)–(5c) are eliminated when all the equations are summed up, which makes the sum $\Phi_1 + \Phi_2 + \Phi_3$ an eigenstate of the Hamiltonian (2).

We consider a pd scattering state of the initial pd momentum p_0, which gives the three-body c.m. energy

$$E = E_{p_0} + E_d, \tag{8}$$

where

$$E_{p_0} = \frac{3\hbar^2}{4m}p_0^2. \tag{9}$$

The integral form of the SSF equation, whose formal derivation is given in Ref. [17], is

$$\Phi_k = \bar{\delta}_{k,3}\Phi^d(\boldsymbol{x}_k)F^C(\boldsymbol{y}_k; p_0, \eta_0) + \mathcal{G}_k(E)\,[\Delta\Phi]_k\,, \tag{10}$$

where $\bar{\delta}_{i,j} = 1 - \delta_{i,j}$; $\Phi^d(\boldsymbol{x})$ is the deuteron state; $F^C(\boldsymbol{y}, p_0, \eta_0)$ is a scattering state in the Coulomb potential $u^C(y)$, which satisfies

$$[T_y(\boldsymbol{y}) + u^C(y)]F^C(\boldsymbol{y}; p_0, \eta_0) = E_{p_0}F^C(\boldsymbol{y}; p_0, \eta_0), \tag{11}$$

with the Coulomb parameter $\eta_0 = \eta(p_0)$ given by Eq. (B2); the operators $\mathcal{G}_k(E)$ are channel Green's functions defined as

$$\mathcal{G}_k(E) \equiv \begin{cases} \dfrac{1}{E + \imath\varepsilon - H_0 - V_k^S - u^C(y_k)} & (k = 1, 2), \\ \dfrac{1}{E + \imath\varepsilon - H_0 - V_3^S - V^C(x_3)} & (k = 3), \end{cases} \tag{12}$$

with the parameter ε being a small positive number to give outgoing waves.

A partial-wave decomposition is performed by introducing an angular function denoted as $|\alpha(\hat{\boldsymbol{x}}, \hat{\boldsymbol{y}})\rangle$,

$$|\alpha(\hat{\boldsymbol{x}}, \hat{\boldsymbol{y}})\rangle = [Y_L(\hat{\boldsymbol{x}}) \otimes Y_\ell(\hat{\boldsymbol{y}})]^{J_0}_{M_0}\,, \tag{13}$$

where L denotes the relative orbital angular momentum of the pair particles, ℓ denotes the orbital angular momentum of the spectator particle, and $J_0(=L+\ell)$ and M_0 denote the total angular momentum of the three particles and its third component, respectively. The set of the quantum numbers (L, ℓ, J_0, M_0) is represented by the index α.

We define complete orthogonal sets of functions describing the angular parts of the three-body system with a state index α and the radial part of the spectator particle with momentum p and angular momentum ℓ,

$$|\mathcal{F}_{k,\underline{\alpha}}\rangle \equiv |\alpha[(\hat{\boldsymbol{x}}_k, \hat{\boldsymbol{y}}_k)]\rangle \times \begin{cases} \sqrt{\dfrac{2}{\pi}}\dfrac{F_\ell[\eta(p), py_k]}{y_k} & (k = 1, 2), \\ \sqrt{\dfrac{2}{\pi}}pj_\ell(py_k) & (k = 3), \end{cases} \tag{14}$$

where $F_\ell(\eta, r)$ is the regular Coulomb function of Eq. (B1) [20,21], $\eta(p)$ is the Coulomb parameter of Eq. (B2), and $j_\ell(r)$ is the spherical Bessel function. The underline implies a dependence on the momentum p. These functions satisfy a complete relation,

$$\int_{\underline{\alpha}} |\mathcal{F}_{k,\underline{\alpha}}\rangle\langle\mathcal{F}_{k,\underline{\alpha}}| = 1, \tag{15}$$

and an orthogonal relation,

$$\langle\mathcal{F}_{k,\underline{\alpha}}|\mathcal{F}_{k,\underline{\alpha}'}\rangle = \delta_{\alpha,\alpha'}\delta(p - p') = \delta_{\underline{\alpha},\underline{\alpha}'}, \tag{16}$$

where $\int_{\underline{\alpha}}$ means $\sum_\alpha \int_0^\infty dp$, and $\langle|\rangle$ integrations over the variables $\hat{\boldsymbol{x}}$ and $\boldsymbol{y}$.

The channel Green's function is decomposed by the complete set to give

$$\mathcal{G}_k(E) = \int_{\underline{\alpha}} |\mathcal{F}_{k,\underline{\alpha}})G_{k,\underline{L}}(\mathcal{F}_{k,\underline{\alpha}}|. \tag{17}$$

Here, $G_{k,\underline{L}}$ is a two-body Green's operator,

$$G_{k,\underline{L}} = \frac{1}{E_q + \imath\varepsilon - T_L(x) - V_k^S(x) - \delta_{k,3}V^C(x)}, \tag{18}$$

where E_q is the energy of the two-body subsystem given by

$$E_q = E - \frac{3\hbar^2}{4m}p^2 = \frac{\hbar^2}{m}q^2, \tag{19}$$

and

$$T_L(x) = -\frac{\hbar^2}{m}\left[\frac{d^2}{dx^2} + \frac{2}{x}\frac{d}{dx} - \frac{L(L+1)}{x^2}\right]. \tag{20}$$

III. COULOMB FORCE EFFECTS IN THE SSF INTEGRAL KERNEL

The SSF integral equation presented in the previous section has the form of an inhomogeneous linear equation. We are going to solve this by applying an iterative method developed in Refs. [8,19] (and references therein) that is called the Method of Continued Fractions (MCF). In general, iterative methods to solve a linear equation require operating the kernel to functions that are given in preceding iterative steps. The MCF algorithm, which is reviewed in Appendix A, also includes such operations as indicated in Eqs. (A8) and (A9). Calculations of the SSF integral kernel consist of two parts: a particle exchange operation and the operation of the Green's functions. Some technical notes on the former part are given in Refs. [22,23] and those on the latter part for the *nd* scattering above the TBT are given in Ref. [10], and are useful also in the *pd* scattering. In this section, we study some problems of the SSF integral kernel proper to the *pd* scattering problem.

A. SSF integral kernel

Let us consider operating the SSF kernel on given functions $\Phi_k(\boldsymbol{x}, \boldsymbol{y})$:

$$\Theta_k(\boldsymbol{x}_k, \boldsymbol{y}_k) \equiv \mathcal{G}_k(E)[\Delta\Phi]_k. \tag{21}$$

The channel Green's function for $k = 1$ or 2, where the pair is a *pn* system, possesses a pole corresponding to the deuteron bound state. To treat this pole, we apply a standard subtraction method in which we use an identity,

$$1 = \sum_{\alpha_0} |\alpha_0\phi^d\rangle\langle\phi^d\alpha_0| + \left(1 - \sum_{\alpha_0} |\alpha_0\phi^d\rangle\langle\phi^d\alpha_0|\right), \tag{22}$$

where $\phi^d(x)$ is the radial part of the deuteron wave function with orbital angular momentum $L_0(=0)$, and the index $\alpha_0 = (L_0, \ell_0, J_0, M_0)$ denotes the three-body partial-wave states that couple to the two-body state with L_0. By applying the identity to $\mathcal{G}_k$, we obtain

$$\begin{aligned}\mathcal{G}_k(E) =& \sum_{\alpha_0} |\alpha_0\phi^d\rangle\breve{G}_{C,\ell_0}(E_{p_0})\langle\phi^d\alpha_0| + \int_{\underline{\alpha}} |\mathcal{F}_{k,\underline{\alpha}})G_{k,\underline{L}}(\mathcal{F}_{k,\underline{\alpha}}| \\ &- \int_{\underline{\alpha}_0} \left|\mathcal{F}_{k,\underline{\alpha}_0}\phi^d\right\rangle \frac{1}{E_q - E_d}\left\langle\phi^d\mathcal{F}_{k,\underline{\alpha}_0}\right| \\ &(k = 1, 2).\end{aligned} \tag{23}$$

Here, $\breve{G}_{C,\ell_0}(E_{p_0})$ is the partial-wave component of the Coulomb Green's function for the outgoing proton,

$$\breve{G}_{C,\ell_0}(E_{p_0}) \equiv \frac{1}{E_{p_0} + \imath\varepsilon - T_{\ell_0}(y) - u^C(y)}, \tag{24}$$

with

$$T_\ell(y) = -\frac{3\hbar^2}{4m}\left[\frac{d^2}{dy^2} + \frac{2}{y}\frac{d}{dy} - \frac{\ell(\ell+1)}{y^2}\right]. \tag{25}$$

The function $\Theta_k(\boldsymbol{x}, \boldsymbol{y})$ thereby can be written as

$$\begin{aligned}&\Theta_k(\boldsymbol{x}, \boldsymbol{y}) \\ &= \begin{cases} \displaystyle\sum_{\alpha_0} |\alpha_0)\,\phi^d(x)\eta^{(e)}_{k,\alpha_0}(y) \\ \quad + \displaystyle\int_{\underline{\alpha}} |\mathcal{F}_{k,\underline{\alpha}})\left[\theta_{k,\underline{\alpha}}(x) - \delta_{\alpha,\alpha_0}\phi^d(x)C_{k,\underline{\alpha}_0}\right] \quad (k = 1, 2), \\ \displaystyle\int_{\underline{\alpha}} |\mathcal{F}_{k,\underline{\alpha}})\theta_{k,\underline{\alpha}}(x) \qquad (k = 3). \end{cases}\end{aligned} \tag{26}$$

Here, the function $\eta^{(e)}_{k,\alpha_0}(y)$ $(k = 1, 2)$ represents an elastic component in the scattering,

$$\eta^{(e)}_{k,\alpha_0}(y) = \int_0^\infty y'^2 dy' \breve{G}_{C,\ell_0}(y, y'; E_{p_0})\omega^{(e)}_{k,\alpha_0}(y'), \tag{27}$$

with

$$\breve{G}_{C,\ell}(y, y'; E_p) \equiv \langle y|\breve{G}_{C,\ell}(E_p)|y'\rangle, \tag{28}$$

and a source function $\omega^{(e)}_{k,\alpha_0}(y)$ given by

$$\begin{aligned}\omega^{(e)}_{k,\alpha_0}(y) &= \langle\phi^d\alpha_0|[\Delta\Phi]_k\rangle \\ &= \langle\phi^d\alpha_0|V_k^S|\Phi_i + \Phi_j\rangle.\end{aligned} \tag{29}$$

The explicit expression of the Green's function $\breve{G}_{C,\ell}(y, y'; E_p)$, Eq. (B5) [20], gives the asymptotic form of $\eta^{(e)}_{k,\alpha_0}(y)$ as

$$\eta^{(e)}_{k,\alpha_0}(y) \underset{y\to\infty}{\to} \frac{e^{\imath\sigma_{\ell_0}(\eta_0)}u^{(+)}_{\ell_0}(\eta_0, p_0 y)}{y} T^{(e)}_{k,\alpha_0}, \tag{30}$$

where $T^{(e)}_{k,\alpha_0}$ is an amplitude defined by

$$T^{(e)}_{k,\alpha_0} = -\left(\frac{4m}{3\hbar^2 p_0}\right)\int_0^\infty dy F_\ell(\eta_0, p_0 y) y \omega^{(e)}_{k,\alpha_0}(y). \tag{31}$$

Above the TBT, the source function $\omega^{(e)}_{k,\alpha_0}(y)$ reveals a long-range behavior of $\mathcal{O}(y^{-5/2})$ even in the case of the *nd* scattering due to the particle exchange with breakup channel. This property was studied to develop a numerical treatment in Ref. [10].

The coefficient $C_{k,\underline{\alpha}_0}$ $(k=1,2)$ and the function $\theta_{k,\underline{\alpha}}(x)$ $(k=1,2,3)$ in Eq. (26) are defined as

$$C_{k,\underline{\alpha}_0} = \frac{1}{E_q - E_d}\langle \phi^d \mathcal{F}_{k,\underline{\alpha}_0} | V_k^S | \Phi_i + \Phi_j \rangle, \tag{32}$$

$$\theta_{k,\underline{\alpha}}(x) = \langle x | G_{k,\underline{L}} | \omega_{k,\underline{\alpha}} \rangle, \tag{33}$$

where a source function $\omega_{k,\underline{\alpha}}(x)$ is composed of a contribution from the short-range potential and one from the Coulomb potentials,

$$\omega_{k,\underline{\alpha}}(x_k) = \omega^S_{k,\underline{\alpha}}(x_k) + \delta_{k,3}\omega^C_{\underline{\alpha}}(x_k), \tag{34}$$

with

$$\begin{aligned}\omega^S_{k,\underline{\alpha}}(x_k) &= (\mathcal{F}_{k,\underline{\alpha}} | V_k^S | \Phi_i + \Phi_j\rangle \\ &= V_k^S(x_k)(\mathcal{F}_{k,\underline{\alpha}} | \Phi_i + \Phi_j\rangle, \end{aligned}\tag{35}$$

$$\begin{aligned}\omega^C_{\underline{\alpha}}(x_3) &= (\mathcal{F}_{3,\underline{\alpha}} | V^C(x_3) - u^C(y_1) | \Phi_1\rangle \\ &\quad + (\mathcal{F}_{3,\underline{\alpha}} | V^C(x_3) - u^C(y_2) | \Phi_2\rangle. \end{aligned}\tag{36}$$

Note that the apparent singularity of $C_{k,\underline{\alpha}_0}$ for $E_q = E_d$, or $p = \sqrt{\frac{4m}{3\hbar^2}(E + |E_d|)}$, [see Eq. (19)] is canceled by that of the function $\theta_{k,\underline{\alpha}}(x)$ arising from the two-body Green's function $G_{k,\underline{L}}$ and therefore the standard quadrature can be applied to perform the p integration of Eq. (26) as far as both terms are treated together as demonstrated in Ref. [10].

In actual calculations of the functions $\theta_{k,\underline{\alpha}}(x)$, we consider an ordinary differential equation that is transformed from Eq. (33),

$$\left[E_q - T_L(x) - V_k^S(x) - \delta_{k,3}V^C(x)\right]\theta_{k,\underline{\alpha}}(x) = \omega_{k,\underline{\alpha}}(x). \tag{37}$$

A boundary condition to get the physical solution of this equation depends on the energy of the two-body subsystem E_q and thus on the integral variable p in Eq. (26) via Eq. (19). According to the sign of E_q, the range of p $(0 \leqslant p < \infty)$ is divided into two regions: (i) $0 \leqslant p \leqslant p_c = \sqrt{\frac{4m}{3\hbar^2}E}$, where $E_q \geqslant 0$, and (ii) $p_c < p < \infty$, where $E_q < 0$. The corresponding boundary conditions for $k = 1, 2$ are

$$\theta_{k,\underline{\alpha}}(x) \underset{x\to\infty}{\propto} \begin{cases} h_L^{(+)}(qx) & (0 \leqslant p \leqslant p_c), \\ h_L^{(+)}(\imath|q|x) & (p_c < p < \infty), \end{cases} \tag{38}$$

where $h_\ell^{(+)}(r)$ is the spherical Hankel function with the outgoing wave. For $k = 3$, where the pp Coulomb potential is acting, we have

$$\theta_{3,\underline{\alpha}}(x) \underset{x\to\infty}{\propto} \begin{cases} \dfrac{u_L^{(+)}(\gamma(q), qx)}{x} & (0 \leqslant p \leqslant p_c), \\ \dfrac{W_{-\gamma(|q|),L+1/2}(2|q|x)}{x} & (p_c < p < \infty), \end{cases} \tag{39}$$

where $\gamma(q)$ is given by Eq. (C6) and $W_{\kappa,\mu}(z)$ is the Whittaker function [21]. We solve Eq. (37) with the previously mentioned conditions by applying the usual techniques we would apply in the two-body problem, for example, the Numerov algorithm [23]. Treatments of Eq. (37) for $k = 1, 2$ in region (i), which are the same as those for the nd scattering, are described in Appendix B of Ref. [10]. While those for the $k = 3$ case, where we need to consider Coulomb force effects, are given in Appendix C of this article.

The asymptotic form of the function $\Theta_k(\boldsymbol{x}, \boldsymbol{y})$ is obtained by evaluating Eq. (26) with the saddle-point approximation [24,25] together with an explicit asymptotic form of $\theta_{3,\underline{\alpha}}(x)$ for $0 \leqslant p \leqslant p_c$ given by Eq. (C26). We notice that the Coulomb force effects appear in the spectator variable $\boldsymbol{y}_k$ for $k = 1, 2$ and in the pair coordinate $\boldsymbol{x}_k$ for $k = 3$. The result is

$$\begin{aligned}\Theta_k(\boldsymbol{x}, \boldsymbol{y}) \underset{x\to\infty}{\to} & -e^{\frac{\pi}{4}\imath}\sum_\alpha |\alpha| \imath^{-L-\ell}\left(\frac{4K_0}{3}\right)^{3/2} \\ & \times \frac{e^{\imath[K_0 R - \delta_{k,3}\gamma(\bar{q})\ln(2\bar{q}x) - \bar{\delta}_{k,3}\eta(\bar{p})\ln(2\bar{p}y)]}}{R^{5/2}} B_{k,\alpha}(\Theta), \end{aligned}\tag{40}$$

where the limit is considered to be taken with x/y being fixed, a hyper radius R and a hyper angle Θ are introduced as

$$R = \sqrt{x^2 + \frac{4}{3}y^2}, \tag{41}$$

$$x = R\cos\Theta, \quad y = \sqrt{\frac{3}{4}}R\sin\Theta, \tag{42}$$

and K_0 and the momenta $\bar{q}$ and $\bar{p}$ are given by

$$K_0 = \sqrt{\frac{m}{\hbar^2}E}, \tag{43}$$

$$\bar{q} = K_0\cos\Theta, \quad \bar{p} = \sqrt{\frac{4}{3}}K_0\sin\Theta. \tag{44}$$

Here, $B_{k,\alpha}(\Theta)$ is a breakup amplitude defined as

$$B_{k,\alpha}(\Theta) = -\frac{1}{\bar{p}}\frac{m}{\hbar^2}\frac{1}{1 - \imath\mathcal{K}_L(\bar{q})}\langle \bar{\psi}_{k,L}(\bar{q}) | \omega_{k,\underline{\alpha}}\rangle, \tag{45}$$

where $\bar{\psi}_{k,L}(x;q)$ is a two-body scattering solution with the standing wave boundary condition and $\mathcal{K}_L(q)$ is a scattering K matrix for the two-body scattering (see Appendix C).

B. Coulomb long-range effects

In solving the differential Eq. (37) numerically, we need to set a value x_M by a condition that the source function $\omega_{k,\underline{\alpha}}(x)$ should vanish so that the solution reaches its asymptotic form given by Eqs. (38) or (39) for $x > x_M$. The range of $\omega_{k,\underline{\alpha}}(x)$ thus is an important issue in our calculations. Equation (35) shows that the range of the short-range potential term $\omega^S_{k,\underline{\alpha}}(x)$ for $k = 1, 2, 3$ is determined by the range of $V_k^S(x)$. Therefore, in the case of $k = 1, 2$, where there is no contribution from the Coulomb term, we set x_M to be a value larger than the range of the 2NP, for example, 10 fm.

In the case of $k = 3$, however, the source function includes the Coulomb term $\omega^C_{\underline{\alpha}}(x_3)$, whose range depends on the factor

$$\begin{aligned}&[V^C(x_3) - u^C(y_1)]\Phi_1(\boldsymbol{x}_1, \boldsymbol{y}_1) + (1 \leftrightarrow 2) \\ &\quad = \left(\frac{1}{x_3} - \frac{1}{y_1}\right)\Phi_1(\boldsymbol{x}_1, \boldsymbol{y}_1) + (1 \leftrightarrow 2).\end{aligned}$$

In our iterative scheme (see Appendix A), the zeroth order of the source function $\omega^{[0]}_{3,\underline{\alpha}}(x_3)$ is calculated by putting $\Phi_1(\boldsymbol{x}_1, \boldsymbol{y}_1) = \Phi^d(\boldsymbol{x}_1)F^C(\boldsymbol{y}_1; p_0, \eta_0)$, in which the magnitude of the variable $\boldsymbol{x}_1$ is restricted within the range of the deuteron

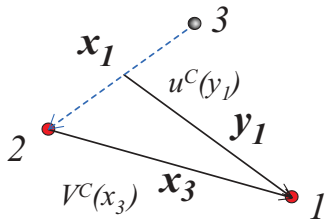

FIG. 2. (Color online) Jacobi coordinates ($\boldsymbol{x}_1$, $\boldsymbol{y}_1$, and $\boldsymbol{x}_3$) to describe the pp Coulomb potential $V^C(x_3)$ and the auxiliary Coulomb potential $u^C(y_1)$.

size. Using an expression given by the definition of the Jacobi coordinates, Eq. (1) (see also Fig. 2),

$$\boldsymbol{y}_1 = \boldsymbol{x}_3 + \tfrac{1}{2}\boldsymbol{x}_1, \tag{46}$$

we can easily show that

$$\frac{1}{x_3} - \frac{1}{y_1} = \frac{1}{x_3} - \frac{1}{\left|\boldsymbol{x}_3 + \frac{1}{2}\boldsymbol{x}_1\right|} \underset{x_3\to\infty}{\to} \mathcal{O}\left(x_3^{-2}\right). \tag{47}$$

The same situation holds for the replacement of $(1 \leftrightarrow 2)$. The source term $\omega^C_{\underline{\alpha}}(x_3)$ therefore is supposed to be a short-range function due to a cancellation between V^C and u^C.

An example of the cancellation is shown in Fig. 3(a), where we plot components of $\omega^{[0]}_{3,\underline{\alpha}}(x_3)$ for a partial-wave state of ${}^1S_0(pp) - s_{1/2}$ and the total three-body angular momentum and parity of $1/2^+$, and $p = 0.30$ fm^{-1} for the pd scattering at incident proton energy $E_p = 13.0$ MeV using the Argonne V_{18} (AV18) 2NP [26]. In the figure, a component due to the 2NP, $\omega^S_{3,\underline{\alpha}}(x_3)$ (the solid curve), and components due to the Coulomb potentials, $\omega^C_{\underline{\alpha}}(x_3)$, including only V^C (the dotted curve) and both of V^C and u^C (the dashed curve) are plotted. For $x_3 < 2$ fm, only the term $\omega^S_{3,\underline{\alpha}}(x_3)$ is plotted because the Coulomb contributions are very small in this region. As shown by the dotted and dashed curves in the figure, the contribution of V^C is well canceled by that of u^C for large values of x_3 in the zeroth-order calculation.

Figure 3(b) shows the components of $\omega^{[1]}_{3,\underline{\alpha}}(x_3)$ calculated from functions $\Phi^{[1]}_k(\boldsymbol{x}_k, \boldsymbol{y}_k)$ that are obtained by the operation of the kernel to the initial state. Once the integral kernel is operated, the resulting functions include the three-body breakup component as expressed by Eq. (40), and thus the range of x_1 in such functions is not restricted to the range of the deuteron. As a result, the cancellation as Eq. (47) is no more expected for higher order calculations. This is demonstrated by the fact that dashed curve in the figure, which denotes the source term $\omega^C_{\underline{\alpha}}(x_3)$ including both of V^C and u^C contributions, remains non-negligible for a large value of x_3.

To include the long-range effect of $\omega^C_{\underline{\alpha}}(x_3)$ as much as possible, one needs to increase the value of x_M much more than 10 fm, which is the standard value in the nd calculation. This makes pd calculations much harder than nd calculations. Because Fig. 3 implies that the source function $\omega_{3,\underline{\alpha}}(x_3)$ is dominated by the 2NP contribution $\omega^S_{3,\underline{\alpha}}(x_3)$, we decide to include the effect of the long-range contribution partially by multiplying $\omega^C_{\underline{\alpha}}(x_3)$ by the cutoff factor

$$e^{-(x_3/R_C)^N} \tag{48}$$

for higher order than the zeroth order in our iterative procedure of the MCF.

The validity of this procedure is examined in Table I, where we compare some results of the pd eigenphase shift and mixing angle parameters in conventions defined in Ref. [27], for a partial-wave state with the total angular momentum and parity of $1/2^+$ calculated with the AV18 potential. In the table, the last column shows the results obtained with the Kohn variational principle (KVP) [28]. The rest of the columns show our calculations. The first column denoted as WC0 shows results calculated by completely neglecting $\omega^C_{\underline{\alpha}}(x_3)$ in all order calculations of the MCF iteration scheme to solve the SSF equation. Calculations with keeping $\omega^C_{\underline{\alpha}}(x_3)$ only for the zeroth order without cutoff but neglecting $\omega^C_{\underline{\alpha}}(x_3)$ for higher order calculations are shown in the second column (WCn). In the third to fifth columns, we show results with the cutoff for the nonzeroth order by choosing $N = 4$ and $R_C = 4$, 6, and 8 fm, respectively. A comparison of the numbers in the table

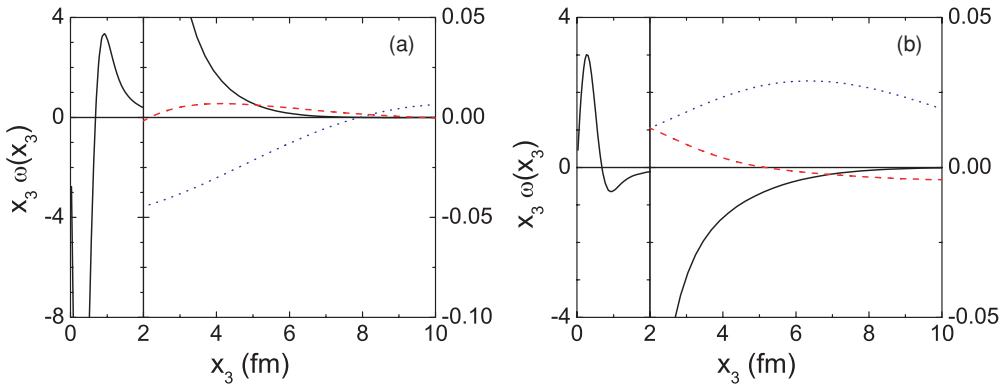

FIG. 3. (Color online) Examples of the source functions (a) for the zeroth-order calulations and (b) for the first-order calculations. The solid curves denote the contribution from the short-range 2NP $\omega^S_{3,\underline{\alpha}}(x_3)$, the dotted curves that from the Coulomb potentials $\omega^C_{\underline{\alpha}}(x_3)$ neglecting the contribution from u^C, and the dashed curves that from $\omega^C_{\underline{\alpha}}(x_3)$ including the contribution from both of V^C and u^C. Note that the scales of the vertical axis change at $x_3 = 2.0$ fm.

TABLE I. The real and complex part of the pd eigenphase shift and mixing angle parameters, which are given in degrees, for the $J^\pi = 1/2^+$ state with the AV18 potential. See the text for the meaning of the calculations.

	WC0	WCn	$N=4$ $R_C=4$ fm	$N=4$ $R_C=6$ fm	$N=4$ $R_C=8$ fm	KVP[a]
$E_p = 5.0$ MeV						
$^4D_{1/2}$	(−5.33, 0.01)	(−5.44, −0.01)	(−5.44, −0.01)	(−5.45, 0.00)	(−5.45, 0.00)	(−5.43, 0.004)
$^4S_{1/2}$	(−42.4, 1.93)	(−42.4, 1.93)	(−41.8, 2.36)	(−41.8, 2.30)	(−41.8, 2.15)	(−41.8, 1.74)
$\eta_{1/2+}$	(0.97, −0.04)	(1.01, −0.03)	(1.05, −0.03)	(1.05, −0.04)	(1.05, −0.04)	(1.05, −0.03)
$E_p = 10.0$ MeV						
$^4D_{1/2}$	(−7.15, 0.24)	(−7.32, 0.21)	(−7.32, 0.22)	(−7.33, 0.22)	(−7.34, 0.22)	(−7.30, 0.24)
$^4S_{1/2}$	(−61.3, 11.6)	(−61.5, 11.5)	(−61.0, 12.4)	(−60.9, 11.9)	(−60.8, 11.9)	(−60.6, 11.7)
$\eta_{1/2+}$	(0.96, 0.03)	(0.98, 0.05)	(1.02, 0.05)	(1.02, 0.04)	(1.01, 0.04)	(1.01, 0.06)

[a]Ref. [28].

indicates that effects due to the neglect of the long-range term $\omega_\alpha^C(x_3)$ in the integral kernel may be an order of a few percent in the phase shift parameters and suggests that the partial inclusion with the cutoff factor with $(N, R_C) = (4, 8$ fm), for example, may produce sufficient results. We remark that the imaginary part of the $^4S_{1/2}$ parameter reveals a rather slow convergence, which might affect scattering observables. This point is discussed later.

IV. NUMERICAL RESULTS

In this section, we present some numerical results obtained by using the formulation described in the previous sections. Technical details of introducing spins' degrees of freedom, 3NFs, etc., are given in Refs. [8,10,22,23]. As a standard 2NF model, we choose the AV18 potential [26]. Three-nucleon partial-wave states, for which the 2NF and 3NFs are active, are restricted to those with total two-nucleon angular momenta $J \leqslant 6$ for bound state calculations and $J \leqslant 4$ for scattering calculations. In scattering calculations, total $3N$ angular momentum is truncated at $J_0 = 19/2$, whereas 3NFs are switched off for $3N$ states with $J_0 > 13/2$.

As described in the previous section, the Coulomb source term $\omega_\alpha^C(x)$ in the SSF integral kernel is treated by multiplying with the cutoff factor Eq. (48) for higher order in the MCF iteration. Comparisons of calculations performed by taking three different sets of (N, R_C) in Table I show that a satisfactory convergence is obtained with parameters of $(N, R_C) = (4, 8$ fm) for elastic observables, and we thus proceed with these parameters, referring to them simply as *pd calculations*. A convergence problem for three-body breakup observables is discussed in a subsection below.

The calculated binding energy of ^{3}H (^{3}He) with the AV18 potential is 7.626 MeV (6.928 MeV), which is underbound by about 1 MeV compared to the empirical value of 8.482 MeV (7.718 MeV). It is well known that a 3NF caused by the exchange of two pions among three nucleons ($2\pi E$-3NF) produces enough attraction to explain the empirical binding energy. In this article, we use a new version of the Brazil $2\pi E$-3NF [11] with a dipole form factor of the cutoff mass parameter Λ, $(\frac{\Lambda^2 - m_\pi^2}{\Lambda^2 + \boldsymbol{q}^2})^2$, for the πNN vertex (BR_Λ). In a combination with the AV18 2NP, Λ is chosen to be 660 MeV ($\mathrm{AV18} + \mathrm{BR}_{660}$) to give the binding energy 8.492 MeV (7.763 MeV) for ^{3}H (^{3}He).

A. Differential cross section in elastic scattering

First, we compare calculations approximately including the pp Coulomb force effects with those of the pd calculations for the differential cross section $\sigma(\theta)$ of the pd elastic scattering, where θ is the scattering angle in the c.m. system. We take two approximate calculations: One is the WC0 calculation, which is presented in the previous section. The other one, denoted as APn, is an approximate calculation in which the scattering amplitude due to the short-range 2NF is replaced by a corresponding nd scattering amplitude [29]. It is expected that the WC0 calculations are better approximated at lower energies because breakup effects are smaller. The APn calculations, however, are expected to be better at higher energies. Figure 4, where WC0 (bold curves) and APn calculations (thin curves) of differential cross sections normalized by those with the pd calculations at $E_p = 5.0$, 10.0, and 28.0 MeV are plotted, looks to exhibit roughly these tendencies. It is remarkable that

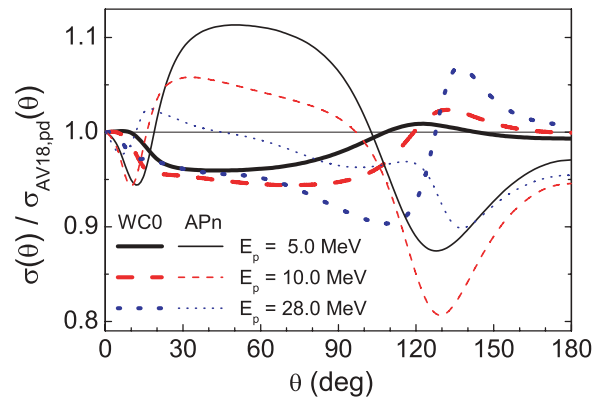

FIG. 4. (Color online) Differential cross section of pd elastic scattering normalized by the pd calculation with the AV18 potential. The bold curves represent the AV18-WC0 calculations, and the thin curves represent the AV18-APn calculations. The solid curves denote calculations at $E_p = 5.0$ MeV, the dashed curves calculations at $E_p = 10.0$ MeV, and the dotted curves calculations at $E_p = 28.0$ MeV.

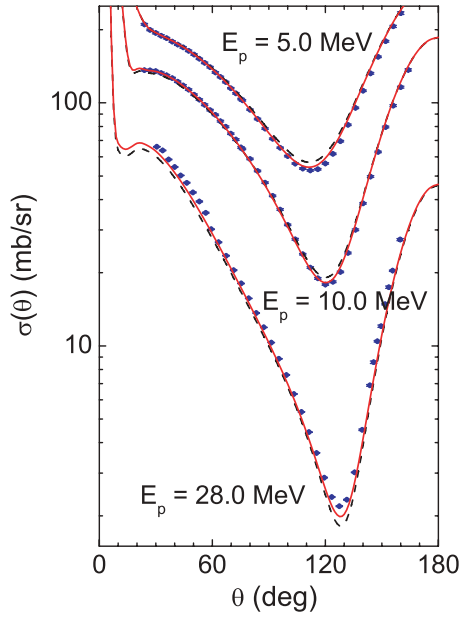

FIG. 5. (Color online) Differential cross sections of pd elastic scattering at $E_p = 5.0$, 10.0, and 28.0 MeV. The dashed curves denote calculations with the AV18 potential and the solid curves those with the AV18 + BR_{660} potential. Experimental data are from Ref. [30] for $E_p = 5.0$ and 10.0 MeV and from Ref. [31] for $E_p = 28.0$ MeV.

deviations of the APn calculations are rather large, about 10% even at backward angles.

In Fig. 5, the pd calculations for $\sigma(\theta)$ of the pd elastic scattering at $E_p = 5.0$, 10.0, and 28.0 MeV are plotted together with experimental data [30,31]. Comparing the calculations with the AV18 potential (the dashed curves) to the experimental data at $\theta \sim 120^\circ$, where $\sigma(\theta)$ takes the minimum, one finds that the calculations overestimate the data at lower energies and underestimate the data at higher energies. The introduction of the $2\pi E$-3NF as shown by the solid curves reduces almost all of the discrepancies at lower energies. This systematic difference between the 2NF calculations and the data, which is referred to as "*Sagara discrepancy,*" was pointed out in Ref. [30] using the APn calculations. To study this discrepancy in detail, we plot a relative discrepancy between the data [30–32] and calculations defined by

$$\Delta_{\min} = \frac{\sigma^{\rm calc}(\theta_{\min}) - \sigma^{\rm exp}(\theta_{\min})}{\sigma^{\rm exp}(\theta_{\min})} \tag{49}$$

in Fig. 6, where $\theta_{\min}$ is the scattering angle where the differential cross section takes the minimum. The pd calculation shows that a systematic discrepancy still remains when effects of the Coulomb force are treated properly, but with shifting transition energy from the overestimation to the underestimation to a higher energy of about $E_p = 20$ MeV as compared to that by the APn calculation, about 5 MeV. This tendency is consistent with the results reported in Refs. [2,4].

B. Phenomenological three-nucleon force

In Ref. [18], it is pointed out that the introduction of the $2\pi E$-3NF causes an undesirable effect to the tensor analyzing

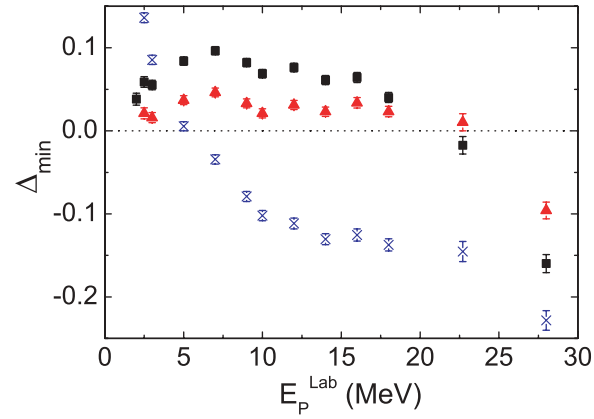

FIG. 6. (Color online) Discrepancy of the pd differential cross section minimum $\Delta_{\min}$ defined in Eq. (49) using the experimental data [30–32]. The solid squares denote the pd calculations with the AV18 potential, the triangles those with the AV18 + BR_{660} potential, and the crosses the APn calculations with the AV18 potential.

power $T_{21}(\theta)$ of the pd elastic scattering at energies below the TBT. Also, the $2\pi E$-3NF is known to have little effect on the vector analyzing power $A_y(\theta)$, for which there exists a rather large discrepancy between experimental data and calculations ("A_y *puzzle*"). These facts, which are also demonstrated in Fig. 7, suggest that the $2\pi E$-3NF is insufficient to comprise a nuclear Hamiltonian in addition to the realistic 2NF. Because no possible mechanism to produce additional 3NF to remedy the previously mentioned defects is established, at the moment a phenomenological 3NF model is introduced [12], which has a form that typical components in 2NP, central, tensor, and spin-orbit components, are modified in the presence of a third nucleon. The explicit form of the 3NF is

$$V^{\rm phe} = \sum_{i<j} e^{-\left(\frac{r_{ik}}{r_G}\right)^2 - \left(\frac{r_{jk}}{r_G}\right)^2} [V_0 + V_T S_T(ij)\hat{P}_{11}] + V_{ls} e^{-\alpha_{ls}\rho} \sum_{i<j} [\ell_{ij} \cdot (S_i + S_j)]\hat{P}_{11}, \tag{50}$$

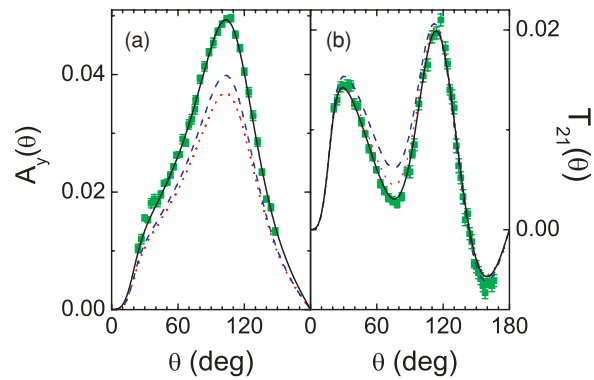

FIG. 7. (Color online) (a) Proton vector analyzing power $A_y(\theta)$ and (b) deuteron tensor analyzing power $T_{21}(\theta)$ of pd elastic scattering at $E_p = 3.0$ MeV. The dotted curves denote calculations with the AV18 potential, the dashed curves those with the AV18 + BR_{660} potential, and the solid curves those with the AV18 + BR_{800} + $V^{\rm phe}$ potential. Experimental data are from Refs. [30,34].

where $S_T(ij)$ is the tensor operator acting between the nucleon pair ij, $\hat{P}_{11}$ is the projection operator to the spin and isospin triplet state of the pair ij, and $\rho^2 = \frac{2}{3}(r_{12}^2 + r_{23}^2 + r_{31}^2)$. The range parameter r_G was taken to be 1.0 fm and α_{ls} to be 1.5 fm^{-1}. In Ref. [12], the strength parameters, V_0, V_T, and V_{ls}, are determined in the following manner: We choose the combination of the AV18 potential for 2NF and a former version of the Brazil model [33] with $\Lambda = 800$ MeV for the $2\pi E$-3NF as a starting interaction, which makes the triton overbound by about 1 MeV. The parameters are decided to reproduce the following observables: the triton binding energy, the vector analyzing power $A_y(\theta)$, and the tensor analyzing power $T_{21}(\theta)$ in pd scattering at $E_p = 3.0$ MeV. The results are $V_0 = 25$ MeV, $V_T = -40$ MeV, and $V_{ls} = -16$ MeV.

In the present work, we use a new version of the Brazil 3NF [11] that is more attractive in the $3N$ bound states than the earlier version [33]. We thus need to retune the value of V_0 to be 36 MeV, but without changing the values of V_T and V_{ls}. The calculated binding energy with this set of potentials (AV18 + BR$_{800}$ + $V^{\rm phe}$) is 8.482 MeV (7.757 MeV) for ^{3}H (^{3}He), and the results for $A_y(\theta)$ and $T_{21}(\theta)$ at $E_p = 3.0$ MeV are shown by solid curves in Fig. 7.

C. Polarization observables in elastic scattering

In Ref. [12], it is shown that the use of the phenomenological 3NF together with the AV18 + BR$_{800}$, which is tuned to reproduce the $3N$ binding energy, $A_y(\theta)$ and $T_{21}(\theta)$ at $E_p = 3.0$ MeV, is also successful in describing the neutron vector analyzing power $A_y(\theta)$ of the nd scattering at higher energies. In Fig. 8, calculations of $A_y(\theta)$ of the pd and nd scattering with the AV18 + BR$_{800}$ + $V^{\rm phe}$ potentials are compared with experimental data at some energies above the TBT [30,34–36]. While the calculations of the nd-$A_y(\theta)$ agree with the experimental data in a manner similar to that in Ref. [12], those of the pd-$A_y(\theta)$ overestimate the data at the maximum region $\theta \sim 130^\circ$ as the energy increases. In another aspect, the calculated difference between the nd- and the pd-$A_y(\theta)$ at the maximum region is decreasing as the energy increases, which is contradictory to the tendency of the experimental data.

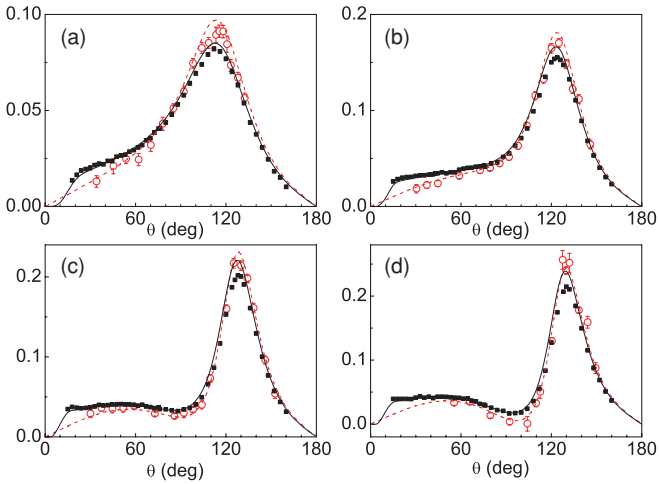

FIG. 8. (Color online) Nucleon vector analyzing power $A_y(\theta)$ of pd and nd elastic scattering at $E_N =$ (a) 5.0 MeV, (b) 10.0 MeV, (c) 14.0 MeV, and (d) 16.0 MeV. Solid (dashed) curves denote pd (nd) calculations with the AV18 + BR$_{800}$ + $V^{\rm phe}$ potential. Experimental data are from Refs. [30,34] for pd (solid squares) and Refs. [35,36] for nd (open circles).

In Fig. 9, calculations of the deuteron tensor analyzing power $T_{21}(\theta)$ of the pd scattering at $E_p = 10.0$ and 28.0 MeV are compared with experimental data [31,37]. As in the case at low energy, the introduction of the $2\pi E$-3NF shifts the calculations in the wrong direction from the experimental data around $\theta = 90^\circ$, and the phenomenological 3NF works to reproduce the data. Another interesting feature appears at $\theta \sim 130^\circ$, where $T_{21}(\theta)$ takes the maximum as follows: Although the calculations with the AV18 potential deviate from the data, those including the 3NFs agree with the data equally. These suggest that $T_{21}(\theta \sim 90^\circ)$ is sensitive to tensor components of nuclear forces and that $T_{21}(\theta \sim 130^\circ)$ is sensitive to central components.

In Fig. 10, energy dependence of the deuteron tensor analyzing power $T_{21}(\theta)$ at $\theta = 90^\circ$ in the pd elastic scattering for calculations with the AV18, AV18 + BR$_{660}$, and AV18 + BR$_{800}$ + $V^{\rm phe}$ potentials is shown in comparison with available data [30,31,34,37]. The figure shows that the introduction of the phenomenological 3NF is still consistent with data at higher energies. It will be interesting to see if further $T_{21}(\theta)$ data at $E_p = 20$ to 30 MeV, where experimental data are missing, are consistent with the calculation or not.

Polarization-transfer coefficients are another interesting observable, and they are sensitive to spin-dependent interactions. In Fig. 11, the polarization-transfer coefficients $K_y^{y'}(\theta)$ of pd and nd elastic scattering at $E_N = 19.0$ MeV are compared with experimental data [38,39]. One interesting point, which has been already remarked upon in Ref. [40], is that the Coulomb force effect in the calculation is opposite to that in the data at $\theta \sim 110^\circ$. In addition, the figure shows that the experimental data indicate that the AV18 + BR$_{660}$ potential is favored over the AV18 + BR$_{800}$ + $V^{\rm phe}$ potential, implying that this observable may be useful in distinguishing various 3NF models that reproduce other observables equally.

D. Breakup cross section

Finally, we show some results for differential cross sections of kinematically complete three-body breakup reactions, ^{2}H$(p,pp)n$ and ^{2}H$(n,nn)^1$H, which are characterized by configurations of three particles in the final state. Here, we discuss four different kinematical conditions that include the following typical configurations, whose experimental data at $E_N = 13.0$ MeV are available for the pd breakup in Ref. [41] and for the nd breakup in Refs. [42,43]:

(i) collinear (COL) configuration, in which three nucleons align on a line with the unobserved nucleon being at rest in the c.m. system;

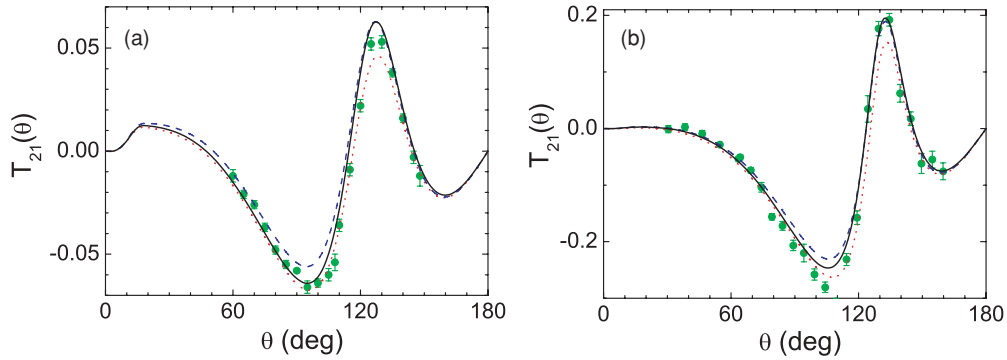

FIG. 9. (Color online) Deuteron tensor analyzing power $T_{21}(\theta)$ of pd elastic scattering at $E_p =$ (a) 10.0 MeV and (b) 28.0 MeV (or equivalently $E_d = 20.0$ and 56.0 MeV, respectively, in a deuteron incident scattering). The dotted curves denote calculations with the AV18 potential, the dashed curves those with the AV18 + BR_{660} potential, and the solid curves those with the AV18 + BR_{800} + V^{phe} potential. Experimental data are from Ref. [37] for $E_p = 10.0$ MeV and Ref. [31] for $E_p = 28.0$ MeV.

(ii) final state interaction (FSI) configuration, in which the relative energy between the unobserved nucleon and one of the observed nucleons is zero;
(iii) space star (SST) configuration, in which three nucleons have equal energies and interparticle angles of 120° in the c.m. system, and the plane spanned by the three nucleons is orthogonal to the beam axis; and
(iv) quasi-free scattering (QFS) configuration, in which the unobserved nucleon is at rest in the laboratory system.

First, we have checked a convergence of the breakup cross sections with respect to the cutoff procedure of the long-range Coulomb force effect with Eq. (48). Calculations with the three parameter sets shown in Table I, namely, $(N, R_C) = (4, 4$ fm), (4, 6 fm), and (4, 8 fm), for the SST and the QFS configurations agree with one another excellently; however, those for the COL and the FSI configurations agree in part as shown in Figs. 12(a) and 12(b).

The visible deviations in Figs. 12(a) and 12(b) appear at a kinematical condition where the relative pn energy is small, that is, $E_{pn} < 0.5$ MeV, which might be caused by a small change in the pp interaction due to our Coulomb treatment. To check this peculiar behavior, we have investigated the dependence of the pn-FSI cross sections in the nd breakup reaction on the neutron-neutron (nn) interaction using two different 2NP models: a charge-independent 2NP, Argonne V_{14} (AV14) [44], in which the nn force is equal to the pn force in the $^1S_0$ state, and its modified version (AV14′) made in Refs. [15,16] by considering a charge-dependent potential to distinguish the nn force from the pn force. Results are shown in Figs. 12(c) and 12(d) that demonstrate that a change in a nn force actually results in non-negligible effects for the pn-FSI cross sections.

Next, as a reference, cross sections of the FSI configuration for the ^{2}H(p,pn)^{1}H and ^{2}H(n,np)n reactions at $E_N =$ 13.0 MeV are plotted in Fig. 13. In this configuration, the pn-FSI cross section occurs around $S = 3$ MeV and the pp-FSI or nn-FSI cross section occurs around $S = 11$ MeV. The

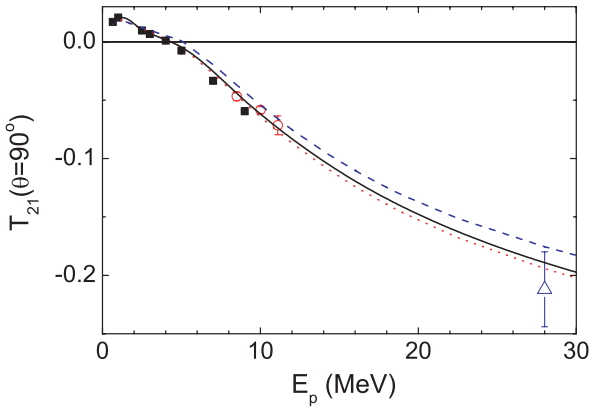

FIG. 10. (Color online) Energy dependence of deuteron tensor analyzing power $T_{21}(\theta = 90°)$ of pd elastic scattering. The dotted curve denotes calculations with the AV18 potential, the dashed curve ones with the AV18 + BR_{660} potential, and the solid curve ones with the AV18 + BR_{800} + V^{phe} potential. Experimental data are from Ref. [34] (squares), Ref. [37] (circles), and Ref. [31] (triangle).

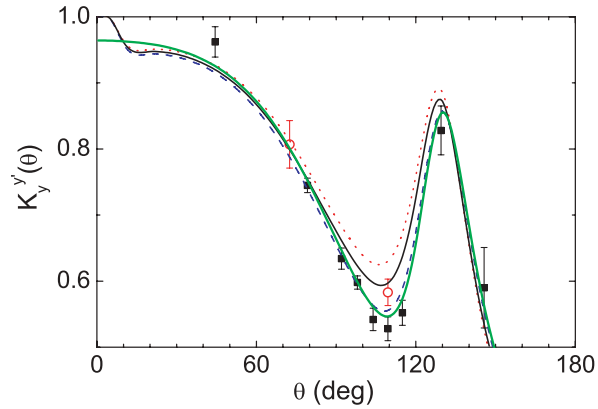

FIG. 11. (Color online) Polarization-transfer coefficient $K_y^{y'}(\theta)$ of pd and nd elastic scattering at $E_N = 19.0$ MeV. The dotted curve denotes the pd calculation with the AV18 potential, the dashed curve the pd calculation with the AV18 + BR_{660} potential, the solid curve the pd calculation with the AV18 + BR_{800} + V^{phe} potential, and the bold curve the nd one with the AV18 + BR_{800} + V^{phe} potential. Experimental data are from Ref. [38] for pd scattering (solid squares) and from Ref. [39] for nd scattering (open circles).

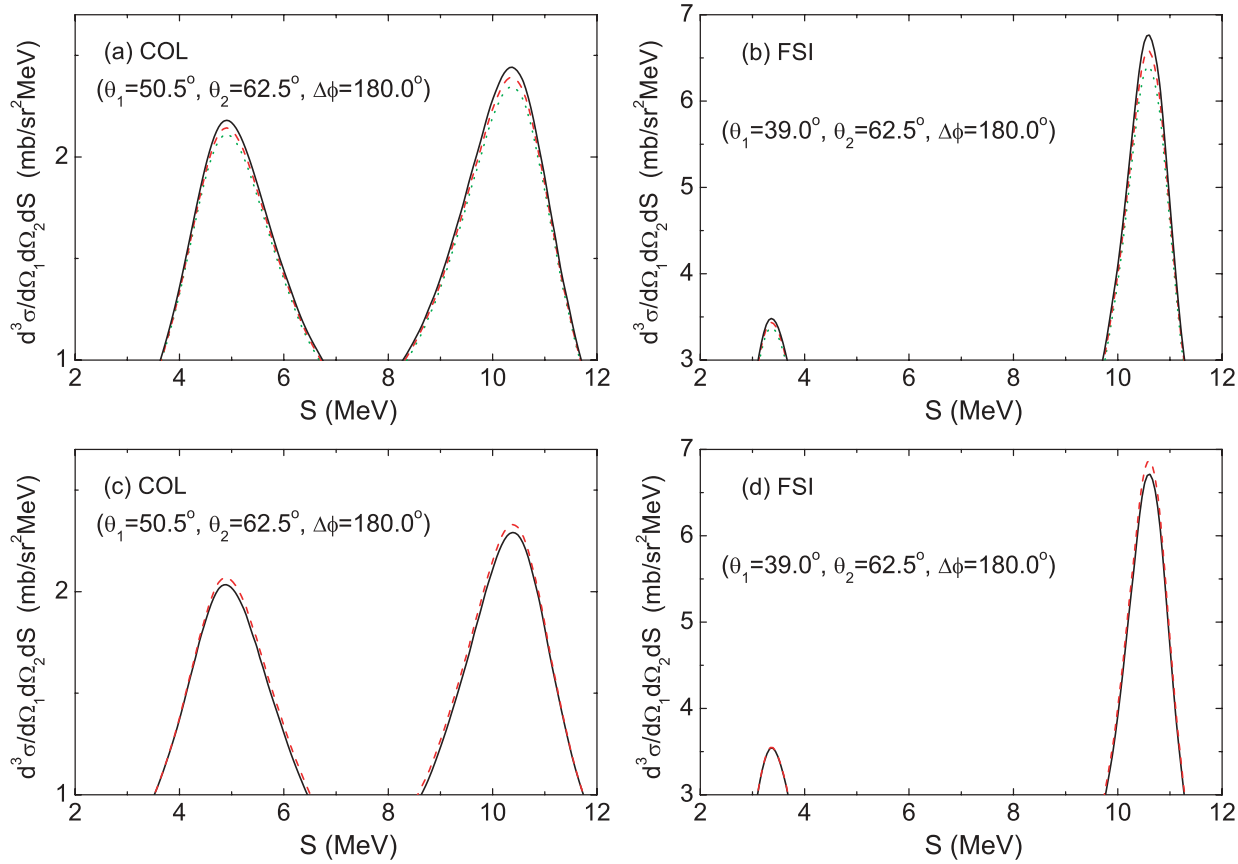

FIG. 12. (Color online) Differential cross sections of pd-breakup reactions (a) for the COL configuration and (b) for the FSI configuration and those of nd-breakup reactions (c) for the COL configuration and (d) for the FSI configuration at $E_N = 13.0$ MeV. In panels (a) and (b), dotted curves denote calculations with $(N, R_C) = (4, 4$ fm) for the AV18 potential, dashed curves denote calculations with $(N, R_C) = (4, 6$ fm), and solid curves denote calculations with $(N, R_C) = (4, 8$ fm). In panels (c) and (d), solid curves denote the calculations with the AV14 potential and dashed curves denote calculations with the AV14′ potential.

pp-FSI cross sections are suppressed by the pp Coulomb force compared to the nn-FSI cross sections, but not completely. This may suggest that we need to improve the Coulomb cutoff procedure possibly by extending the range of the cutoff function to treat the pp-FSI cross section more correctly.

From these considerations, we conclude that our calculations successfully converge for most of breakup configurations, except for possibly a limited region with the relative energy of two nucleons being close to zero.

In Fig. 14, results of the pd- and nd-breakup cross sections for the above four configurations with the AV18 and the AV18 + BR_{660} potentials are compared with the experimental data. Effects of the Coulomb force are visible for the COL, SST, and QFS configurations, but not for the FSI configuration, which is consistent with the result of the momentum space calculations [6]. However, effects of the $2\pi E$-3NF are small except for the QFS configurations. In the momentum space approach [6], 3NF effects are incorporated alternatively in terms of an explicit introduction of a single virtual Δ-isobar excitation. The results also show that effects of the Δ-isobar in the breakup cross sections are small for the COL, FSI, and SST configurations and are visible for the QFS configuration.

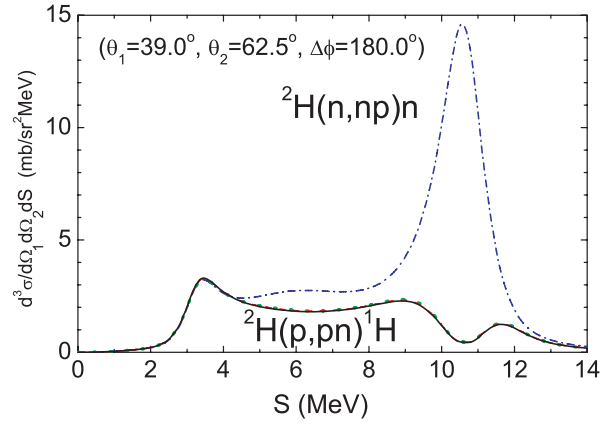

FIG. 13. (Color online) Differential cross sections of $^2\mathrm{H}(p, pn)^1\mathrm{H}$ and $^2\mathrm{H}(n, np)n$ reactions for the FSI configuration at $E_N = 13.0$ MeV with the AV18 potential. The dotted curve denotes calculations for the pd-breakup reaction with $(N, R_C) = (4, 4$ fm), the dashed curve denotes calculations for the pd-breakup reaction with $(N, R_C) = (4, 6$ fm), and the solid curve denotes calculations for the pd-breakup reaction with $(N, R_C) = (4, 8$ fm). The dot-dashed curve denotes the cross section for the nd-breakup reaction.

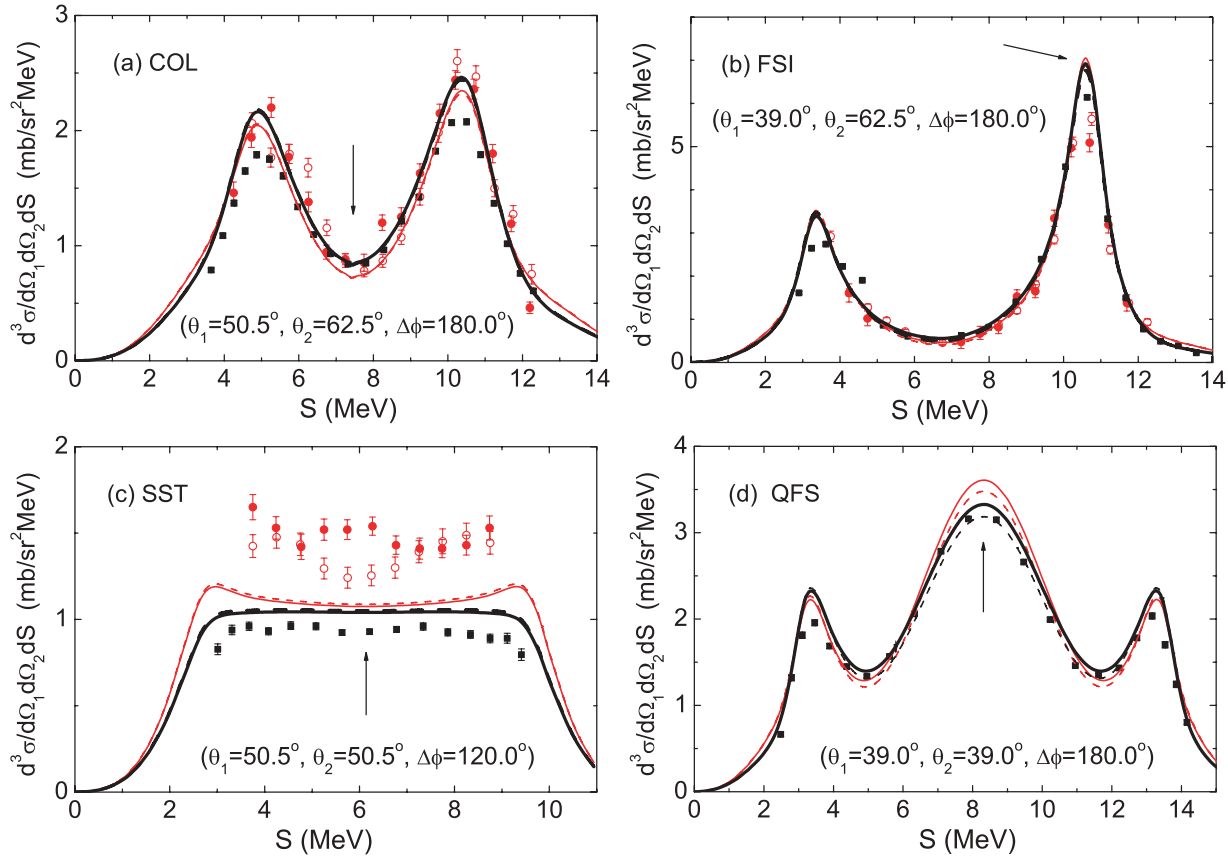

FIG. 14. (Color online) Differential cross sections of pd- and nd-breakup reactions for (a) the COL configuration, (b) the FSI configuration, (c) the SST configuration, and (d) the QFS configuration at $E_N = 13.0$ MeV. The bold curves are for pd scattering and the thin curves for nd scattering. The dashed curves denote the calculations with the AV18 potential, and the solid curves those with the AV18 + BR_{660} potential. Experimental data are from Ref. [41] (solid squares) for pd scattering and Ref. [42] (open circles) and Ref. [43] (solid circles) for nd scattering. The arrows indicate the kinematical points that match the typical configurations.

V. SUMMARY

We presented a practical method to solve the pd scattering problem at energies above the threshold of the deuteron breakup to accommodate effects of the long-range pp Coulomb force as accurately as possible. Although the convergence with respect to the cutoff procedure of the long-range Coulomb force effect is left as a future problem at a particular kinematical condition of breakup reactions, a successful convergence was obtained for elastic observables and for most of the kinematical regions in breakup reactions. We thereby calculated some observables in pd and nd reactions at energies up to 30 MeV. Effects of the two-pion-exchange 3NF and the phenomenological 3NF to reproduce low-energy $3N$ observables were examined for pd observables at higher energies, and then some discrepancies between calculations and experimental data as well as inconsistencies between calculations and data with respect to Coulomb force effects were observed. Studies searching for realistic mechanisms to produce interaction models to remedy these defects with calculations by the formalism presented in this article are now in progress.

ACKNOWLEDGMENTS

The author thanks H. Paetz gen Schieck for providing experimental data. The numerical calculations in this article are supported by the Research Center for Computing and Multimedia Studies, Hosei University.

APPENDIX A: METHOD OF CONTINUED FRACTION

In this appendix, we summarize the MCF algorithm to solve the SSF equation (see Refs. [8,19] and references therein). Let us consider solving the linear integral equation

$$|\Phi) = |F) + \mathcal{G}\Delta\,|\Phi)\,. \tag{A1}$$

In the notation of the present work, $|\Phi)$ and $|F)$ are expressed as vectors,

$$|\Phi) = \begin{pmatrix} \Phi(\boldsymbol{x}_1, \boldsymbol{y}_1) \\ \Phi(\boldsymbol{x}_2, \boldsymbol{y}_2) \\ \Phi(\boldsymbol{x}_3, \boldsymbol{y}_3) \end{pmatrix}, \tag{A2}$$

$$|F) = \begin{pmatrix} \Phi^d(\boldsymbol{x}_1)F^C(\boldsymbol{y}_1; p_0, \eta_0) \\ \Phi^d(\boldsymbol{x}_2)F^C(\boldsymbol{y}_2; p_0, \eta_0) \\ 0 \end{pmatrix}, \tag{A3}$$

and $\mathcal{G}$ and Δ are expressed as matrices

$$\mathcal{G} = \begin{bmatrix} \mathcal{G}_1(E) & 0 & 0 \\ 0 & \mathcal{G}_2(E) & 0 \\ 0 & 0 & \mathcal{G}_3(E) \end{bmatrix}, \tag{A4}$$

$$\Delta = \begin{bmatrix} 0 & V_1^S & V_1^S \\ V_2^S & 0 & V_2^S \\ V_3^S + V^C(x_3) - u^C(y_1) & V_3^S + V^C(x_3) - u^C(y_2) & 0 \end{bmatrix}. \tag{A5}$$

Setting $|F^{[0]})$ and $\mathcal{G}^{[0]}$ as

$$|F^{[0]}) = |F), \tag{A6}$$

$$\mathcal{G}^{[0]} = \mathcal{G}, \tag{A7}$$

we define $|F^{[i]})$ and $\mathcal{G}^{[i]}$ $(i = 1, 2, \ldots)$ as follows:

$$|F^{[i]}) = \mathcal{G}^{[i-1]}\Delta|F^{[i-1]}), \tag{A8}$$

$$\mathcal{G}^{[i]} = \mathcal{G}^{[i-1]} - |F^{[i]})\frac{1}{(F^{[0]}|\Delta|F^{[i-1]})}(F^{[0]}|$$

$$= \mathcal{G}^{[0]} - \sum_{j=1}^{i} |F^{[j]})\frac{1}{(F^{[0]}|\Delta|F^{[j-1]})}(F^{[0]}|. \tag{A9}$$

Introducing $|\Phi^{[i]})$ $(i = 0, 1, 2, \ldots)$ as solutions of

$$|\Phi^{[i]}) = |F^{[i]}) + \mathcal{G}^{[i]}\Delta|\Phi^{[i]}), \tag{A10}$$

we can derive a relation between $|\Phi^{[i]})$ and $|\Phi^{[i+1]})$,

$$|\Phi^{[i]}) = |F^{[i]}) + |\Phi^{[i+1]})\frac{(F^{[0]}|\Delta|F^{[i]})}{(F^{[0]}|\Delta|F^{[i]}) - T^{[i+1]}}. \tag{A11}$$

Here, amplitudes $T^{[i]}$ $(i = 0, 1, 2, \ldots)$ are defined as

$$T^{[i]} = (F^{[0]}|\Delta|\Phi^{[i]}), \tag{A12}$$

which satisfy

$$T^{[i]} = \frac{(F^{[0]}|\Delta|F^{[i]})^2}{(F^{[0]}|\Delta|F^{[i]}) - T^{[i+1]}}. \tag{A13}$$

Calculations of an Nth order approximation start by regarding $|F^{[N]})$ as $|\Phi^{[N]})$:

$$|\Phi^{[N]}) = |F^{[N]}) \tag{A14}$$

and thereby

$$T^{[N]} = (F^{[0]}|\Delta|F^{[N]}). \tag{A15}$$

Then, using Eqs. (A11) and (A13) backward, we calculate $|\Phi^{[N-1]})$, $|\Phi^{[N-2]})$, ..., successively until $|\Phi^{[0]})$ as the Nth order approximation for $|\Phi)$.

APPENDIX B: COULOMB FUNCTIONS

In this appendix, we summarize formulas of functions related to spectator functions modified by the Coulomb potential. See Ref. [21] for details.

Let $F_\ell(\eta(p), py)$ and $G_\ell(\eta(p), py)$ be the regular and irregular Coulomb functions that satisfy

$$\left[T_\ell(y) + \frac{e^2}{y}\right] y_\ell[\eta(p), py] = \left(\frac{3\hbar^2}{4m}p^2\right) y_\ell[\eta(p), py], \tag{B1}$$

where $y_\ell[\eta(p), py]$ is ether $F_\ell[\eta(p), py]$ or $G_\ell[\eta(p), py]$, and

$$\eta(p) = \frac{2m}{3\hbar^2}\frac{e^2}{p}. \tag{B2}$$

A scattering state for the Coulomb potential $\frac{e^2}{y}$ with energy $\frac{3\hbar^2}{4m}p^2$ is written as

$$F^c[\boldsymbol{y}; \boldsymbol{p}, \eta(p)] = 4\pi \sum_{\ell,m} \imath^\ell Y_\ell^{m*}(\hat{\boldsymbol{p}})Y_\ell^m(\hat{\boldsymbol{y}}) \times e^{\imath\sigma_\ell[\eta(p)]}\frac{F_\ell[\eta(p), py]}{py}, \tag{B3}$$

where $\sigma_\ell(\eta)$ is the Coulomb phase shift,

$$\sigma_\ell(\eta) = \arg\Gamma(\ell + 1 + \imath\eta). \tag{B4}$$

The analytical form of the Green's function, Eq. (28), is given by

$$\breve{G}_{C,\ell}(y, y'; E_p) = -\frac{4m}{3\hbar^2}p\frac{e^{\imath\sigma_\ell[\eta(p)]}u_\ell^{(+)}[\eta(p), py_>]}{py_>} \times \frac{F_\ell[\eta(p), py_<]}{py_<}, \tag{B5}$$

where $u_\ell^{(\pm)}(\eta, r)$ is defined as

$$u_\ell^{(\pm)}(\eta, r) = e^{\mp\imath\sigma_\ell(\eta)}\left[G_\ell(\eta, r) \pm \imath F_\ell(\eta, r)\right], \tag{B6}$$

giving the asymptotic form as

$$u_\ell^{(\pm)}(\eta, r) \underset{r\to\infty}{\to} \exp\left[\pm\imath(r - \eta\ln 2r - \ell\pi/2)\right]. \tag{B7}$$

APPENDIX C: GREEN'S OPERATOR

In this appendix, we first review two-body Green's operators and then describe how to calculate Eq. (33) for the case of $k = 3$ and $E_q > 0$.

We define Green's operators for the outgoing $(+)$ and the incoming $(-)$ boundary conditions with a potential consisting of a short-range potential $V^S(x)$ and a long-range Coulomb potential $V^C(x)$ as

$$G_L^{(\pm)} = \frac{1}{E_q \pm \imath\varepsilon - T_L(x) - V^S(x) - V^C(x)}, \tag{C1}$$

$$G_{C,L}^{(\pm)} = \frac{1}{E_q \pm \imath\varepsilon - T_L(x) - V^C(x)}, \tag{C2}$$

which satisfy the resolvent relations

$$G_L^{(\pm)} = G_{C,L}^{(\pm)} + G_L^{(\pm)}V^S G_{C,L}^{(\pm)} = G_{C,L}^{(\pm)} + G_{C,L}^{(\pm)}V^S G_L^{(\pm)}. \tag{C3}$$

Two-body scattering wave functions corresponding to the outgoing and the incoming boundary conditions $|\psi_L^{(\pm)}\rangle$ satisfy the (partial-wave) Lippmann-Schwinger equations

$$|\psi_L^{(\pm)}\rangle = |\hat{F}_L\rangle + G_{C,L}^{(\pm)}V^S|\psi_L^{(\pm)}\rangle, \tag{C4}$$

where $\hat{F}_L[\gamma(q), qx]$ is a reduced Coulomb function defined by

$$\hat{F}_L[\gamma(q), qx] \equiv \frac{F_L[\gamma(q), qx]}{qx}, \tag{C5}$$

with

$$\gamma(q) = \frac{me^2}{2\hbar^2 q}. \tag{C6}$$

For later use, we define the reduced Coulomb functions $\hat{G}_L(\gamma(q), qx)$ and $\hat{u}_L^{(\pm)}(\gamma(q), qx)$ similar to Eq. (C5).

Using Eq. (C3), we see that a formal solution of Eq. (C4) is written as

$$|\psi_L^{(\pm)}\rangle = |\hat{F}_L\rangle + G_L^{(\pm)} V^S |\hat{F}_L\rangle. \tag{C7}$$

It is convenient to use the principal values of the two-body Green's operators defined as

$$\mathcal{P}G_L = \mathcal{P}\frac{1}{E_q - T_L(x) - V^S(x) - V^C(x)}, \tag{C8}$$

$$\mathcal{P}G_{C,L} = \mathcal{P}\frac{1}{E_q - T_L(x) - V^C(x)}. \tag{C9}$$

As is $G_{C,L}^{(\pm)}$, the analytical form of $\mathcal{P}G_{C,L}^{(\pm)}$ is known and these operators are related as

$$G_{C,L}^{(\pm)} = \mathcal{P}G_{C,L} \mp \imath q \frac{m}{\hbar^2} |\hat{F}_L\rangle\langle\hat{F}_L|. \tag{C10}$$

A scattering wave function corresponding to $\mathcal{P}G_{C,L}$, namely, standing wave solution $|\bar{\psi}_L\rangle$, satisfies

$$|\bar{\psi}_L\rangle = |\hat{F}_L\rangle + \mathcal{P}G_{C,L} V^S |\bar{\psi}_L\rangle, \tag{C11}$$

and a formal solution of this is given as

$$|\bar{\psi}_L\rangle = |\hat{F}_L\rangle + \mathcal{P}G_L V^S |\hat{F}_L\rangle. \tag{C12}$$

From the standing wave solution, the outgoing and the incoming solutions are obtained as

$$|\psi_L^{(\pm)}\rangle = \frac{1}{1 \mp \imath \mathcal{K}_L} |\bar{\psi}_L\rangle, \tag{C13}$$

where $\mathcal{K}_L$ is the scattering K matrix defined by

$$\mathcal{K}_L = -q \frac{m}{\hbar^2} \langle \hat{F}_L | V | \bar{\psi}_L \rangle, \tag{C14}$$

which becomes $\tan\delta$ with a phase shift parameter δ. Using the relations above, one obtains a relation between $G_L^{(\pm)}$ and $\mathcal{P}G_L$ as

$$G_L^{(\pm)} = \mathcal{P}G_L \mp \imath q \frac{m}{\hbar^2} |\bar{\psi}_L\rangle \frac{1}{1 \mp \imath \mathcal{K}_L} \langle \bar{\psi}_L|, \tag{C15}$$

which reduces to Eq. (C10) if $V(x)$ is 0, leading to $\bar{\psi}_L(x) = \hat{F}_L[\gamma(q), qx]$ and $\mathcal{K}_L = 0$.

Next, we discuss the asymptotic form of the Green's function.

Using the resolvent equation, Eq. (C3), the formal solutions, Eqs. (C7) and (C12), and the asymptotic forms of the Coulomb Green's functions, which are obtained from their analytical forms,

$$G_{C,L}^{(\pm)} \to -q \frac{m}{\hbar^2} e^{\pm \imath \sigma_L} |\hat{u}_L^{(\pm)}\rangle \langle \hat{F}_L|, \tag{C16}$$

$$\mathcal{P}G_{C,L} \to q \frac{m}{\hbar^2} |\hat{G}_L\rangle \langle \hat{F}_L|, \tag{C17}$$

we obtain the asymptotic form of the Green's functions,

$$G_L^{(\pm)} \to -q \frac{m}{\hbar^2} e^{\pm \imath \sigma_L} |\hat{u}_L^{(\pm)}\rangle \langle \psi_L^{(\mp)}|, \tag{C18}$$

$$\mathcal{P}G_L \to q \frac{m}{\hbar^2} |\hat{G}_L\rangle \langle \bar{\psi}_L|. \tag{C19}$$

Finally, we describe how to calculate Eq. (33) for $k = 3$, which we write simply as

$$\theta(x) = \langle x | G_L^{(+)} | \omega \rangle. \tag{C20}$$

Using Eq. (C15), one can write $\theta(x)$ as

$$\theta(x) = \bar{\theta}(x) - \imath q \frac{m}{\hbar^2} \bar{\psi}_L(x) \frac{1}{1 - \imath \mathcal{K}_L} \langle \bar{\psi}_L | \omega \rangle, \tag{C21}$$

where a new function $\bar{\theta}(x)$ is defined by

$$\bar{\theta}(x) = \langle x | \mathcal{P}G_L | \omega \rangle. \tag{C22}$$

From Eq. (C19), the asymptotic form of $\bar{\theta}(x)$ can be written as

$$\bar{\theta}(x) \underset{x\to\infty}{\to} q \frac{m}{\hbar^2} \hat{G}_L[\gamma(q), qx] \langle \bar{\psi}_L | \omega \rangle. \tag{C23}$$

In actual calculation, the function $\bar{\theta}(x)$ is obtained by solving the ordinary differential equation

$$[E_q - T_L(x) - V^S(x) - V^C(x)]\bar{\theta}(x) = \omega(x) \tag{C24}$$

with the boundary condition

$$\bar{\theta}(x) \underset{x\to\infty}{\propto} \hat{G}_L[\gamma(q), qx]. \tag{C25}$$

These relations give the asymptotic form of $\theta(x)$ as

$$\theta(x) \underset{x\to\infty}{\to} e^{+\imath\sigma_L} \hat{u}_L^{(+)}[\gamma(q), qx] \frac{1}{1 - \imath \mathcal{K}_L} \left(-q \frac{m}{\hbar^2} \right) \langle \bar{\psi}_L | \omega \rangle. \tag{C26}$$

[1] A. Kievsky, S. Rosati, and M. Viviani, Phys. Rev. Lett. **82**, 3759 (1999).

[2] A. Kievsky, M. Viviani, and S. Rosati, Phys. Rev. C **64**, 024002 (2001).

[3] L. D. Faddeev, Zh. Eksp. Teor. Fiz. **39**, 1459 (1961) [Sov. Phys. JETP **12**, 1014 (1961)].

[4] E. O. Alt, A. M. Mukhamedzhanov, M. M. Nishonov, and A. I. Sattarov, Phys. Rev. C **65**, 064613 (2002).

[5] A. Deltuva, A. C. Fonseca, and P. U. Sauer, Phys. Rev. C **71**, 054005 (2005).

[6] A. Deltuva, A. C. Fonseca, and P. U. Sauer, Phys. Rev. C **72**, 054004 (2005).

[7] A. Deltuva, A. C. Fonseca, and P. U. Sauer, Phys. Rev. C **73**, 057001 (2006).

[8] T. Sasakawa and S. Ishikawa, Few-Body Syst. **1**, 3 (1986).

[9] S. Ishikawa and T. Sasakawa, Few-Body Syst. **1**, 143 (1986).
[10] S. Ishikawa, Few-Body Syst. **40**, 145 (2007).
[11] S. Ishikawa and M. R. Robilotta, Phys. Rev. C **76**, 014006 (2007).
[12] S. Ishikawa, Phys. Rev. C **75**, 061002(R) (2007).
[13] T. Sasakawa and T. Sawada, Phys. Rev. C **20**, 1954 (1979).
[14] T. Sasakawa, H. Okuno, and T. Sawada, Phys. Rev. C **23**, 905 (1981).
[15] Y. Wu, S. Ishikawa, and T. Sasakawa, Phys. Rev. Lett. **64**, 1875 (1990); **66**, 242(E) (1991).
[16] Y. Wu, S. Ishikawa, and T. Sasakawa, Few-Body Syst. **15**, 145 (1993).
[17] S. Ishikawa, Few-Body Syst. **32**, 229 (2003).
[18] S. Ishikawa, M. Tanifuji, and Y. Iseri, Phys. Rev. C **67**, 061001(R) (2003).
[19] S. Ishikawa, Nucl. Phys. **A463**, 145c (1987).
[20] A. Messiah, *Quantum Mechanics* (Dover, New York, 1999).
[21] M. Abramowitz and I. A. Stegun, Eds., *Handbook of Mathematical Functions* (Dover, New York, 1965).
[22] T. Sawada, S. Ishikawa, and T. Sasakawa, Sci. Rep. Tohoku Univ. Ser. 8 **3**, 165 (1982).
[23] T. Sawada and T. Sasakawa, Sci. Rep. Tohoku Univ. Ser. 8 **4**, 1 (1983).
[24] T. Sasakawa and T. Sawada, Suppl. Prog. Theor. Phys. **61**, 61 (1977).
[25] M. R. H. Rudge and M. J. Seaton, Proc. R. Soc. A **283**, 262 (1965).
[26] R. B. Wiringa, V. G. J. Stoks, and R. Schiavilla, Phys. Rev. C **51**, 38 (1995).
[27] D. Hüber, J. Golak, H. Witała, W. Glöckle, and H. Kamada, Few-Body Syst. **19**, 175 (1995).
[28] M. Viviani, A. Kievsky, and S. Rosati, Few-Body Syst. **30**, 39 (2001).
[29] P. Doleschall, W. Grüebler, V. König, P. A. Schmelzbach, F. Sperisen, and B. Jenny, Nucl. Phys. **A380**, 72 (1982).
[30] K. Sagara, H. Oguri, S. Shimizu, K. Maeda, H. Nakamura, T. Nakashima, and S. Morinobu, Phys. Rev. C **50**, 576 (1994).
[31] K. Hatanaka, N. Matsuoka, H. Sakai, T. Saito, K. Hosono, Y. Koike, M. Kondo, K. Imai, H. Shimizu, T. Ichihara, K. Nisimura, and A. Okihana, Nucl. Phys. **A426**, 77 (1984).
[32] W. Grüebler, V. König, P. A. Schmelzbach, F. Sperisen, B. Jenny, R. E. White, F. Seiler, and H. W. Roser, Nucl. Phys. **A398**, 445 (1983); F. Sperisen, W. Grüebler, V. König, P. A. Schmelzbach, K. Elsener, B. Jenny, C. Schweizer, J. Ulbricht, and P. Doleschall, *ibid.* **A422**, 81 (1984).
[33] H. T. Coelho, T. K. Das, and M. R. Robilotta, Phys. Rev. C **28**, 1812 (1983).
[34] S. Shimizu, K. Sagara, H. Nakamura, K. Maeda, T. Miwa, N. Nishimori, S. Ueno, T. Nakashima, and S. Morinobu, Phys. Rev. C **52**, 1193 (1995).
[35] C. R. Howell, W. Tornow, K. Murphy, H. G. Pfutzner, M. L. Roberts, A. Li, P. D. Felsher, R. L. Walter, I. Slaus, P. A. Treado, and Y. Koike, Few-Body Syst. **2**, 19 (1987).
[36] K. Fujita, Doctoral thesis, Kyushu University, 1999; K. Sagara (private communication).
[37] M. Sawada, S. Seki, K. Furuno, Y. Tagishi, Y. Nagashima, J. Schimizu, M. Ishikawa, T. Sugiyama, L. S. Chuang, W. Grüebler, J. Sanada, Y. Koike, and Y. Taniguchi, Phys. Rev. C **27**, 1932 (1983).
[38] L. Sydow, S. Vohl, S. Lemaître, H. Patberg, R. Reckenfelderbäumer, H. Paetz gen Schieck, W. Glockle, D. Hüber, and H. Witała, Few-Body Syst. **25**, 133 (1998).
[39] P. Hempen, P. Clotten, K. Hofenbitzer, T. Köble, W. Metschulat, M. Schwindt, W. von Witsch, L. Wätzold, J. Weltz, W. Glöckle, D. Hüber, and H. Witała, Phys. Rev. C **57**, 484 (1998).
[40] A. Kievsky, S. Rosati, and M. Viviani, Phys. Rev. C **64**, 041001(R) (2001).
[41] G. Rauprich, S. Lemaître, P. Niessen, K. R. Nyga, R. Reckenfelderbäumer, L. Sydow, and H. Paetz gen Schieck, Nucl. Phys. **A535**, 313 (1991).
[42] J. Strate, K. Geissdorfer, R. Lin, W. Bielmeier, J. Cub, A. Ebneth, E. Finckh, H. Friess, G. Fuchs, K. Gebhardt, and S. Schindler, Nucl. Phys. **A501**, 51 (1989).
[43] H. R. Setze, C. R. Howell, W. Tornow, R. T. Braun, D. E. González Trotter, A. H. Hussein, R. S. Pedroni, C. D. Roper, F. Salinas, I. Šlaus, B. Vlahović, R. L. Walter, G. Mertens, J. M. Lambert, H. Witała, and W. Glöckle, Phys. Rev. C **71**, 034006 (2005).
[44] R. B. Wiringa, R. A. Smith, and T. L. Ainsworth, Phys. Rev. C **29**, 1207 (1984).